BENCHMARK TEST OF CUSTOMARY VIGVs WITH OPEN BLADE TIPS AND HUB

R. G. Frank[1] - C. Wacker[2] - Dragan Kožulović[1] - R. Niehuis[1]

[1] Institute of Jet Propulsion
Bundeswehr University Munich
85577 Neubiberg, Germany,
roman.frank@unibw.de

[2] MAN Energy Solutions SE
13507 Berlin, Germany

ABSTRACT

Remarkable efforts have been made to improve the part load compressor operation by a broadened, more efficient working range of variable inlet guide vanes (VIGVs). Though axial VIGVs with either open blade tips or hub are state of-the-art, a direct comparison of both basic vane designs has hardly been considered. VIGVs with hub promise a more efficient flow deflection by avoided blade tip vortices, an improved radial guidance of the flow, and the shift of stall effects towards lower stagger angles by increased averaged blade Reynolds numbers. At the same time, the hub goes with shortcomings such as the losses induced by the struts and wall-blade interactions at the blade tips. To identify whether the expected advantages outweigh the drawbacks, the performance of two, customary VIGVs with and without hub were juxtaposed. Investigations were carried out by five-hole probe wake field traverses and oil film flow visualisations. The full low loss working range was covered by a sufficient range of investigated stagger angles. Whereas the vane configuration with open blade tips proved superiority at high stagger angles, the vane with hub becomes worthwhile at successively reduced stagger angles. From a fluid mechanical perspective, the hub is hence recommended if a wide load range is frequently requested by the compressor application.

KEYWORDS

VARIABLE INLET GUIDE VANES, OPEN BLADE TIPS, HUB, SWIRLED DUCT FLOW

NOMENCLATURE

c	Chord length, blade [m]
d_1	Hub diameter at the VIGV inlet [m]
d_2	Hub diameter at the VIGV outlet [m]
D_1	Casing diameter of VIGV inlet [m]
D_2	Casing diameter of VIGV outlet[m]
M	Local Mach number [-]
$\bar{M}$	Mean averaged inlet Mach number [-]
p	Static pressure [Pa]
p_t	Total pressure [Pa]
q	Dynamic pressure [Pa]
$\bar{r}$	r relative to local pipe radius [-]
r	Radial axis [m]
R	Specific gas constant [J/(kg·K)]
Re_D	Integral Reynolds number [-]
Re_c	Local Reynolds number [-]
s	Chord length, strut [m]
T	Temperature [K]
β_S	Stagger angle [°]
$\Delta\beta$	Circumferential flow deflection [°]
γ	Heat capacity ratio [-]
ζ	Total pressure loss coefficient [-]
$\bar{\Theta}$	Circumferential angle per pitch angle [-]
μ	Dynamic viscosity [kg/(m·s)]
ρ	Density [kg/m^3)]
	Sub-/Superscripts
ref	Integral reference of the VIGV with open blade tips at β_S = 90°
Θ, r	Mass averaged over Θ, r
	Abbreviations
a_1	Measurement plane at the VIGV inlet
b_1	Measurement plane at the VIGV exit
VIGV	Variable inlet guide vane

1 Introduction

The progressive increase of fluctuating, renewable energy sources in the electricity mix scrutinises the traditional approach to operate plants primarily in the most energy efficient operating point. In market conditions of significant supply fluctuations, a flexible plant operation becomes increasingly important. Price fluctuations on the spot and balancing markets can hence be exploited as outlined by Sauer et al. (2019). Due to high power ratings and a wide application in industry, turbocompressors are a particularly suitable application for a supply-oriented machine operation, see Sauer et al. (2022). Load changes of such compressors are largely performed by the pre-whirl control via VIGVs. Comparable broad surge and choke limits along with high efficiencies and high specific isentropic heads are thereby ensured. Exemplary compressor maps are provided by Fister (1986) and Simon et al. (1987). The working principle of the pre-whirl control is outlined by Mohseni et al. (2012).

To further extend the efficient operating range of the compressor, VIGVs with high aerodynamic efficiency over a wide range of stagger angles are considered crucial. Open flow separation has to be avoided longest possible. The main approach to face the limitations of conventional VIGVs with typical symmetric blades as sketched in Figure 1(a) has been the optimisation of the blade geometry. Efforts to improve the blade's deflection characteristics have been made by either chambered or split, tandem configurations, e.g. Sanz et al. (1985), Stark and Böhle (1990), Mohseni et al. (2012), and Händel et al. (2015). The annular vane design, in turn, has hardly been in focus although the minimum chord length c and the correlating minimum local Reynolds number Re_c can be increased by a reduced blade height of vanes with hub as illustrated in Figure 1. In this way, the onset of initial open flow separation effects is ought to be shifted towards lower stagger angles β_S. A favourable radial guidance of the flow is moreover facilitated. Uncertainty remains regarding the effects of the varied flow conditions at the blade tips and the aerodynamic drag of the additional struts and the hub body. Ishino et al.'s (1999) stage tests of VIGV configurations with and without hub revealed an improved part load operation with hub at the cost of slightly decreased efficiencies at full load. A variation of the blade height was not considered, yet. To incorporate the potential advantage of an increased minimum Re_c and to improve the understanding of the underlying flow effects in the VIGV cascade, the following study was performed.

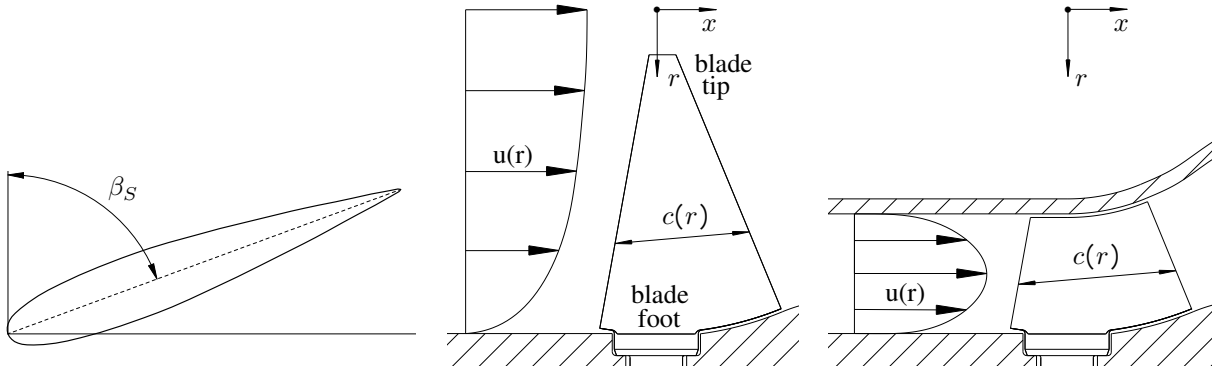

(a) Sketch of the blade geometry* (b) Vane with open blade tips* (c) Vane with hub

Figure 1: Sketch of the blade geometry and the distribution of the velocity u and the chord length c along the radius r, * Frank et al. (2022b)

Investigated VIGVs

Two different VIGV configurations were investigated. The first with open blade tips has been introduced by Frank et al. (2021). The second features a hub instead of the central blow hole. Both cascades are illustrated in Figure 2. Each vane features eleven customary, symmetric blades, an inlet diameter of D_1 = 317 mm, and a spherical casing respectively hub contour in the region downstream the blade shafts, which prevents dispensable clearance between the blade and the wall as shown by Coppinger and Swain (2000). In the present case, the clearance equals 0.32% relative to the inlet diameter. The untwisted, homothetic blades follow one contour. In order to enable the full closing of the VIGV, the blade solidity equals slightly less than one. The blade height of the VIGV with hub is 40% of the configuration with open blade tips. The strut design is closely related to the blade geometry. Inclined rear edges are considered to reduce the dynamic, aerodynamic load on the inducer. Four struts are located directly upstream of four VIGV blades. An impression of the contour of the hub and casing is provided in Figure 3. The hub covers 40% of the inlet cross section compared to 2.5% of the central blow hole of the configuration with open blade tips. Whereas the cross section surface of the VIGV with open blade tips is reduced by 32.7% between in- and outlet cross section a_1 and b_1, see Figure 3, the constriction is only 4.8% if the hub is applied. The casing contour still remains equal. Hubs are usually applied in rather small machines as the relative size of the blow hole increase disproportionally. Both VIGVs were kindly provided by MAN Energy Solutions SE.

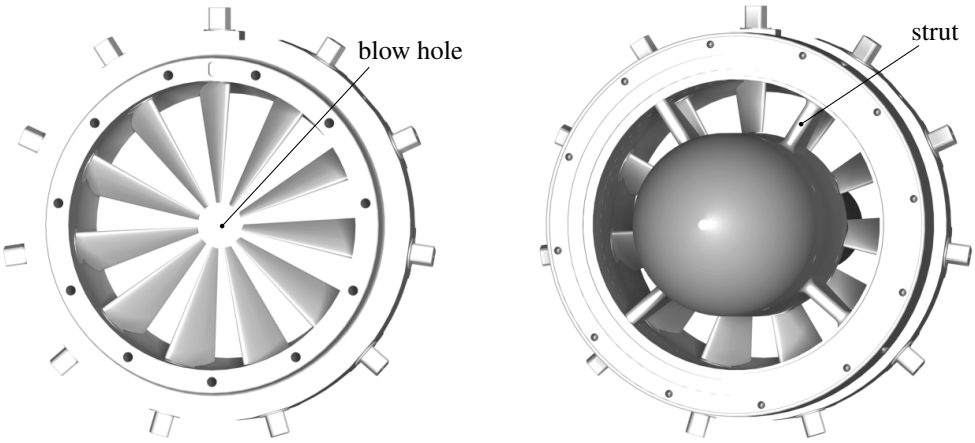

(a) VIGW with open blade tips* (b) VIGV with hub

Figure 2: The two investigated VIGV designs, * Frank et al. (2020)

Experimental Methodology

The investigations have been performed at the VIGV test facility of the University of the Bundeswehr Munich, see Frank et al. (2020). All experiments were conducted at constant, low subsonic and turbulent flow conditions. The averaged Mach and the Reynolds number equal

$$\bar{M} = \frac{4}{\pi} \frac{\dot{m}}{p_{a_1}\left(D_1^2 - d_1^2\right)} \sqrt{\frac{RT}{\gamma}} = 0.125 \tag{1}$$

and

$$Re_D = \frac{\rho \bar{u} D_1}{\mu} = \frac{4}{\pi} \frac{\dot{m}}{D_1^2 - d_1^2} \frac{D_1}{\mu} = 1.16 \times 10^6 \tag{2}$$

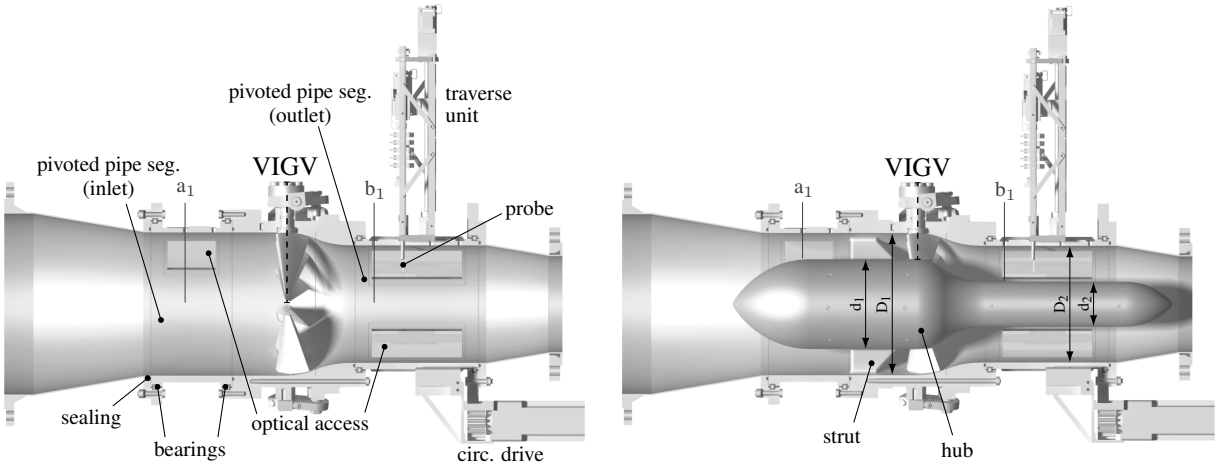

(a) Vane with open blade tips, Frank et al. (2020)

(b) Vane with hub

Figure 3: Measurement section of the test facility with VIGVs with open blade tips or hub

at the inlet cross section a_1 as outlined in Figure 3. The diameter D_1 refers to the casing dimension at the VIGV inlet, d_1 to the corresponding hub diameter. If no hub is applied, d_1 is zero. Assuming constant temperature and pressure levels, all experiments were performed at constant incoming mass flow rates $\dot{m}$ per unit area. The mass flow rates were measured by orifice plates downstream the VIGV. A turbulence level of Tu = 0.67% has been recorded by 1D hot wire anemometry in a_1 upstream the VIGV configuration with open blade tips.

Despite constant mean averaged values of the operating point $\bar{M}$ and Re_D, the radial distribution of $M(r)$ and $Re_c(r)$ shown in Figure 4 is different for both VIGVs. The data are based on a pneumatic wall tap and five-hole probe measurements recorded in cross section a_1. Details are outlined by Frank et al. (2020). Due to a varying velocity distribution for both VIGVs, the level of the local blade Reynolds number $Re_c(r)$ is slightly increased for the configuration with hub, see Figure 4(b). By the blocking of the core region and the avoided short chord lengths c, low values of Re_c at normalised radii $\bar{r}$ < 0.63 are moreover avoided.

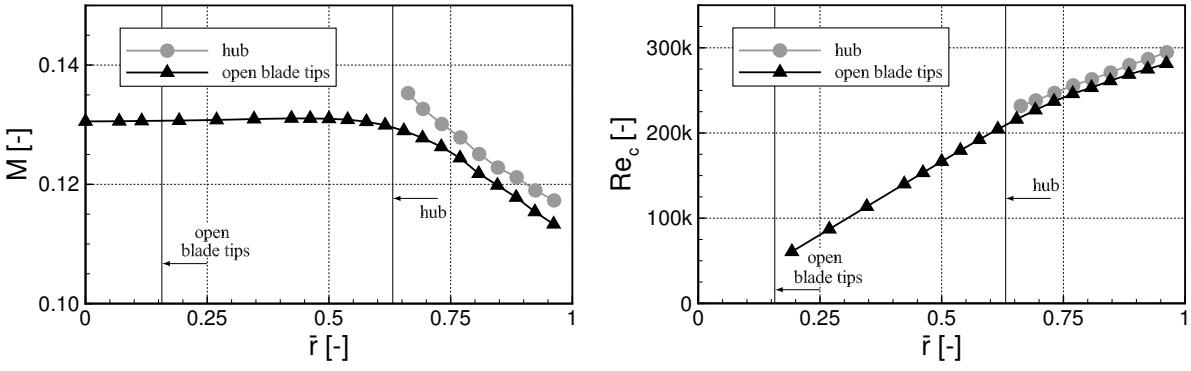

(a) M along $\bar{r}$

(b) Re_c along $\bar{r}$, adopted from Frank et al. (2021)

Figure 4: The local distribution of M and Re_c along the blade height, cross section a_1

To quantify the performance of each VIGV configuration, the total pressure loss coefficient

$$\zeta = \frac{p_{t1} - p_{t2}}{q} \tag{3}$$

and the circumferential flow deflection $\Delta\beta$ are the key variables. To this end, five-hole probe measurements were performed in cross section b_1 ($0.61D_1$) downstream of the blade shaft axis. The total pressure p_{t1} refers to the flow field in b_1 without implemented blades. For p_{t2}, the blades were applied. The final total pressure loss $p_{t1} - p_{t2}$ is based on the correlation of both measurements according to Frank et al. (2021). An impact of the strut wakes in p_{t1} is avoided by rotating the struts off the current circumferential probe position. To enable a distance from the circumferential strut position of at least 1.5 pitches, one strut got removed. Losses induced by struts are hence considered by the correlation of the measurements without and with installed blading. Losses induced by the hub body, in turn, are not fully covered. The dynamic pressure q is based on Eq. 1, the static pressure in a_1, and the equations of isentropic flow.

The investigated stagger angles of β_S = 50° to 90° include the limits of an efficient VIGV operation. The domain of the five-hole probe wake field measurements covers two pitches for the VIGV with open blade tips. If a hub is applied, three pitches are resolved. Despite the lack of perfect circumferential symmetry of the four struts per eleven blades, the chosen domain is considered sufficiently representative. Dependent on the gradients in the wake field, the domain was resolved with 1250 to 1700 measurement points. In the following wake fields, each measurement is indicated by a black dot. Five-hole probe measurements closer than 5 mm to the hub or casing were not taken to avoid off-calibration flow conditions.

In addition to the probe measurements, oil film flow visualisations were performed on the hub and the suction side of the blade. Based on the shear stresses acting on the mixture of hydraulic oil and fluorescent pigments, surface flow effects are visualised. The pictures were recorded after wind tunnel operation. During the post-processing, the colours were inverted and put to a monochrome scale. Hence, black represents the fluorescent particles. For the VIGV with open blade tips, the analysis of the pictures could be substantiated by video recordings during the wind tunnel operation. With hub, the optical access was, however, limited. Further details regarding the procedure are outlined Frank et al. (2022a).

2 Results and discussion

2.1 Local total pressure losses

The distribution of the total pressure losses of the VIGV with open blade tips has previously been published by Frank et al. (2021). The reference value ζ_{ref} was thereby introduced as the integral loss at β_S = 90°. The analysis of the corresponding wake field as shown in Figure 5(a) revealed a straight region of profile losses (i) downstream the blades. Only very light endwall losses (ii), supposedly due to horseshoe vortices, can be detected in the measurement domain near the casing, yet. If β_S is reduced by 20° to β_S = 70°, the primary losses (i) increase as shown in Figure 5(b). Due to varying angular velocities along $\bar{r}$, the flow field is now deflected in circumferential direction. Unlike at β_S = 90°, losses by endwall effects (ii) become substantial. This must be caused by the growing passage, trailing, and clearance vortices induced by an increased flow deflection. At $\bar{r} \approx 0.2$, blade tip losses (iii) are moreover identified. With successively decreased stagger angles of β_S = 60° and 50°, the previously described effects intensify as shown in Figure 5(c) and (d). The locally limited losses based on previous blade tip effects are, however, displaced by a successively intensifying and widening ring shaped loss region (iv). The emerging effects (iv) are ascribed to a stall cell or an open flow separation, which first sets in at the blade tips and successively expands towards larger radii at decreased stagger angles. Such behaviour has been predicted by Händel et al.'s (2014) linear cascade measurements. An accumulation of the fluid flow of high loss (iv) at low radii is moreover plausible. Higher

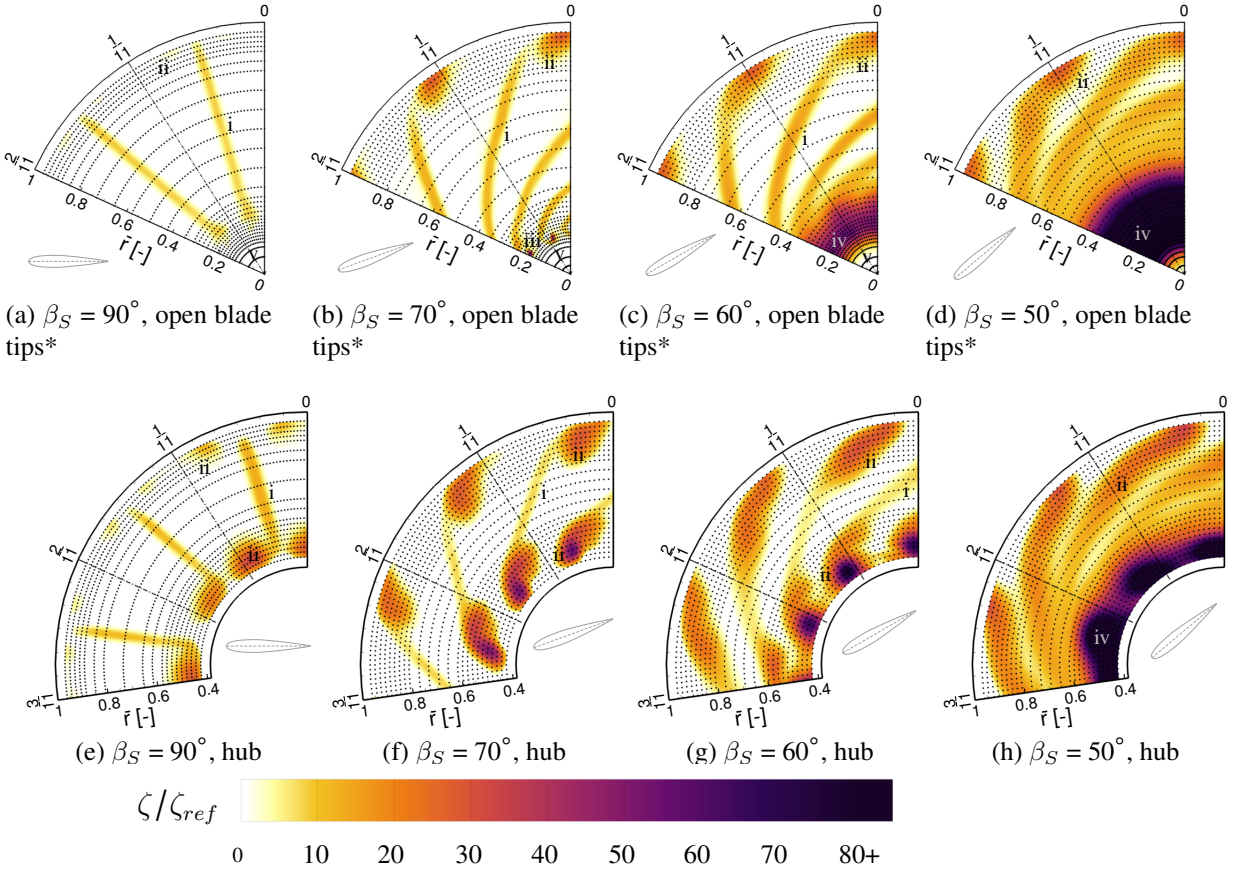

Figure 5: The total pressure loss coefficient ζ/ζ_{ref} in the wake field of the VIGV with open blade tips and hub (i: profile losses, ii: wall-blade interactions, iii: blade tip effects, iv: open flow separation effects, v: straight blow hole flow), * Frank et al. (2021)

total pressure losses correlate with a lowered momentum. The flow downstream a stall cell is hence pushed towards the region of low static pressure in the centre of the swirled flow.

Variations of the loss characteristics are certainly expected if a hub is installed. Additional losses ought to arise from the struts as well as the endwall and clearance effects at the blade tips. Increased minimum local Reynolds numbers Re_c by the reduced blade height are supposed to prevent open flow separation for a wider range of stagger angles. Potential flow separation effects at the casing or the wall may also cause losses. Due to constraints of the correlation of total pressure losses by reference measurements downstream the VIGV as described by Frank et al. (2021), the loss effects at the hub and casing can not be fully resolved. This includes the locally limited, closed flow separation III at the hub as illustrated in Figure 6. For the sake of an adequate radial correlation, the bias of the observed flow separation is still accepted.

The distribution of the losses in the wake field of the configuration with hub are outlined in Figure 5(e) to (h). The impact of the struts becomes distinct in Figure 5(e) at β_S = 90° already. Whereas the straight profile losses (i) between 1/11 ≤ $\bar{\Theta}$ ≤ 3/11 are comparable to the losses of the configuration with open blade tips, the profile losses in the first pitch are increased by the upstream strut body. Distinct loss regions, induced by secondary flow effects, are moreover present to both sides of the profile losses. For the open blade tip configuration shown in Figure 5(a), the losses induced by the horseshoe vortex are considered to be mostly

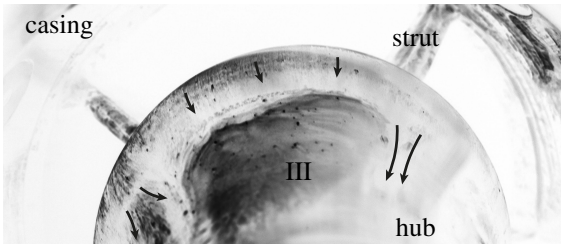

Figure 6: The separation bubble III at the hub without installed blading, rear perspective

hidden outside the measurement domain. A radial shift of the effects near the casing is assumed for the hub configuration by the varied radial guidance of the flow and the lower reduction of the cross section area along the VIGV. The loss regions near the hub, in turn, feature considerably increased losses compared to the secondary losses near the casing. One reason for the higher losses as well as the asymmetry of the effects at the hub, might be the interference of the endwall vortices with the flow separation at the hub contour as outlined in Figure 6.

With decreased stagger angles, the regions of loss can still be divided in an elongated, deflected region of profile losses and the circular spots near the hub and the casing. The lower intensity of the profile losses with hub compared to the open blade tips is explained by an increased radial shift of the streamlines, which locally impedes the correlation of the total pressure losses with and without applied blades. Integral losses as presented in the following are still considered largely unaffected by this bias. The loss regions at the hub consistently remain more pronounced than at the casing. Due to its disappearance, the separation bubble at the hub can not be accounted for this effect at $\beta_S \leq 70^\circ$ anymore. Here, an increased share of the clearance vortex, which is not constrained by the blade shaft at the blade tips, is one potential reason for the higher losses. The development of a blade surface vortex as discussed at the end of the next section is another. Although losses successively increase with lower stagger angles, a clear ring shaped loss region is not observed at $\beta_S = 60^\circ$, yet. A successful shift of the incipient open flow separation by avoided short chord lengths is hence to be assumed. Due to a sharp increase of the total pressure losses at $\beta_S = 50^\circ$, a reasonable low loss operation of the vane is still as unlikely for 50° as it has been for the VIGV with open blade tips.

2.2 Oil film flow visualisations

Though the wake fields in Figure 5 are a useful indicator, the informative value regarding the flow phenomena in the vane remains incomplete. For solidified conclusions, oil film flow visualisations as illustrated in Figure 7 were performed on the blades' suction surface. At first, the visualisation of the configuration with open blade tips shown in the Figures 7(a) to (d) are assessed. The recorded characteristics correlate well with previous assumptions. At $\beta_S \geq 70^\circ$, see Figure 7(a) and (b), open flow separation effects are not present, yet. Instead, a closed flow separation bubble III is identified by the bright surface area along the blade height. The interrelation of the closed flow separation and the bright surface area is confirmed by video recordings of the oil flow. The lack of fluorescent particles within the region of the closed flow separation trades back to a locally enhanced tip facing oil flow in the separation bubble. With a decreased stagger angle, the separation bubble III moves upstream towards the leading edge. A separated-flow transition from 0 to IV via III as identified in preceding linear cascade

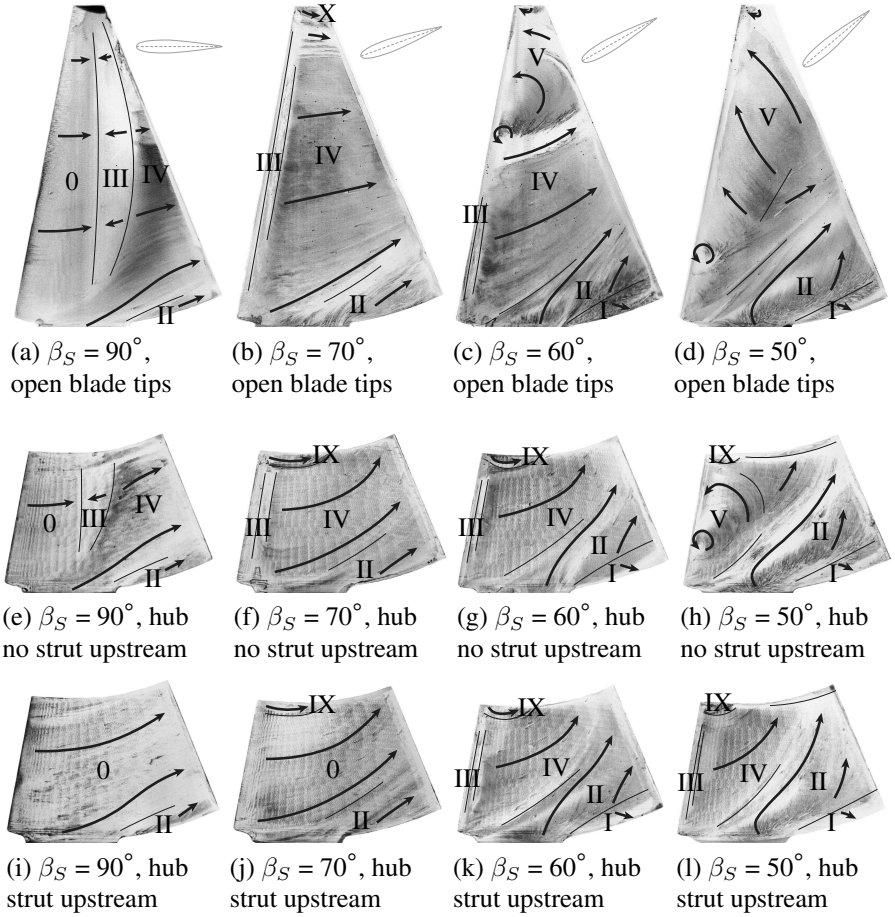

(a) β_S = 90°, open blade tips
(b) β_S = 70°, open blade tips
(c) β_S = 60°, open blade tips
(d) β_S = 50°, open blade tips
(e) β_S = 90°, hub no strut upstream
(f) β_S = 70°, hub no strut upstream
(g) β_S = 60°, hub no strut upstream
(h) β_S = 50°, hub no strut upstream
(i) β_S = 90°, hub strut upstream
(j) β_S = 70°, hub strut upstream
(k) β_S = 60°, hub strut upstream
(l) β_S = 50°, hub strut upstream

Figure 7: Suction side oil film flow visualisations of the symmetric blade with open blade tips (0: attached incoming flow, I: clearance vortex, II: endwall effects, III: closed flow separation, IV: attached flow downstream of III, V: detached flow, X: blade tip vortex)

measurements by Händel et al. (2013) is highly likely.

At β_S = 60°, the previously assumed open flow separation V is confirmed by Figure 7(c). The two counterrotating vortices of a stall cell as found by e.g. Weihs and Katz (1983) or Winkelmann and Barlow (1980) develop on the surface of the blade tip region. Additional recordings at β_S = 65° and 55° illustrated the onset of the stall cell at β_S > 65° and proved the successively increased share of the affected blade height with lower stagger angles. The vortex of the stall cell closer to the blade foot is certainly more pronounced. Its counterpart at the blade tip remains weak. Considering the rise of a laminar open flow separation with low local Reynolds numbers Re_c as outlined in literature, e.g. Hourmouziadis (1989), and Händel's (2016) experiments on a linear cascade of the same blade, separation is assumed to be laminar for the annulus cascade. The white stripe between the attached flow IV and the stall cell V in Figure 7(c) is caused by an increased oil flow. At β_S = 50°, the flow is largely detached. The remaining attached fluid flow is mostly ascribed to the cross flow component induced by the endwall effects II.

With decreasing stagger angles, see Figure 5(a) to (d), the endwall effects II cover an increasing share of the suction surface. At β_S = 90°, only a light radial flow deflection towards the blade tip is identified at the blade foot. The curvature of the casing is therefore accounted.

The further increase of the cross flow II with increased flow deflection complies well with the mechanism of the passage vortex, e.g. Taylor (1968) or Sieverding (1985). A clear identification of the suction side leg of the horseshoe vortex as shown by Sharma and Butler (1987) has not been possible. Either the contrast of the pictures is insufficient or the suction side leg detaches from the blade surface and orbits around the passage vortex, e.g. Sieverding (1985). In addition to the endwall effects, a counterrotating vortex I is identified near the casing at $\beta_S \leq 60^\circ$. The pattern is ascribed to clearance effects between the wall and the blade as outlined by Sjolander (1997). Comparable clearance effects have also been observed downstream the blade shaft by Tesch et al. (2014). The identification of footprints of the blade tip vortex, in turn, is more challenging. Only at $\beta_S = 70^\circ$, a deflected surface flow X is found at the blade tip. An identical surface flow pattern, which arises from the blade tip vortex could be confirmed by in-house RANS simulations. At $\beta_S < 70^\circ$, footprints of the blade tip vortex X are not identified anymore. The vortex must be either suppressed or displaced by the stall cell.

The visualisations of the blades without an upstream strut as illustrated in Figure 7(e) to (h) largely resemble the previously discussed visualisations of the configuration with open blade tips in (a) to (d). Especially at $\beta_S \geq 60^\circ$, the flow visualisations with hub are almost equal to a cut-off version of the blades with open blade tips. The closed flow separation III is identified again. In accordance with the previous configuration, the length of the bubble reduces and the position shifts upstream with lower stagger angles. At $\beta_S = 60^\circ$, the deploying stall cell of the blades with open blade tips is indeed prevented by the increased minimum chord length. At 50°, the flow detaches. The significant increase of the losses in Figure 5(h) is therefore well explained. The region affected by clearance and endwall effects, I and II, does not differ significantly from the configuration with open blade tips. Shape and size remain almost equal.

The oil film flow visualisations of the blades in the wake of one of the four struts as illustrated in Figure 7(i) to (l) feature significantly varying footprints of flow transition compared to the blades without an upstream strut. A closed flow separation III is not present at stagger angles of $\beta_S = 90^\circ$ and 70°. It is firstly identified at $\beta_S = 60^\circ$. At 50°, the flow does not detach, yet. Open flow separation was firstly identified by additional oil film flow visualisations at $\beta_S = 40^\circ$. The increased turbulence level within the strut wake represents a reasonable cause for the deviations from the blades without an upstream strut. The impact of the turbulence level on the laminar-turbulent transition has been pointed out by Mayle (1991). With increased turbulence levels, the limits of the bypass and the separated-flow transition are shifted towards lower Reynolds numbers. Open flow separation is hence avoided for an increased range of stagger angles. At $\beta_S \geq 70^\circ$, the separated-flow transition would be replaced by the bypass transition. Natural transition or even a fully laminar flow are unlikely due to the curved contour of the blade, adverse pressure gradients on the suction side, and the increased turbulence level.

The flow structures near the hub have not been addressed, yet. A locally limited region IX with U-shaped streamlines is observed near the blade tips at $\beta_S < 90^\circ$ regardless of an upstream strut. With decreased stagger angles, the region becomes smaller and moves upstream. Based on the likewise forward shifted suction peak of the profile flow with lower β_S, see Händel (2016), a clearance vortex might be accounted for IX.

Moreover, the consistent radial deflection of the attached suction side flow O/IV towards the hub in Figure 7(e) to (l) indicates flow effects, which are rather uncommon in axial machines. Typically, a suction side surface flow towards the blade mid-height would be expected by the passage vortex. The observed tip facing surface flow, in turn, reminds to the blade surface vortex in a centrifugal impeller as outlined by Eckardt (1976). In the case of a radial flow deflection

in the rotor, an additional vortex develops as the fluid in the blade's boundary layer is pushed inwards on the curved flow path. Figure 8(a) illustrates this effect for a VIGV blade. The driving forces of the vortex are outlined by Taylor (1968) (fairly constant radial static pressure gradients and an inviscid flow are supposed), and correspond in essence to the origin of the passage vortex. The oil film flow visualisation of the surface flow on the hub in Figure 8(b) confirms the presence of the additional vortex structure Y next to the passage vortex II. The picture is recorded from the rear perspective at $\beta_S = 60^\circ$. The noted increase of the losses (ii) near the hub in Figure 5(f) and (g) might also trace back to the additional vortex structure Y. A further influence of the tip clearance, which supposedly intensifies the vortex Y, has been pointed out before. At the casing, in turn, the flow deflection in the blade's boundary layer must be aligned with the sense of rotation of the passage vortex.

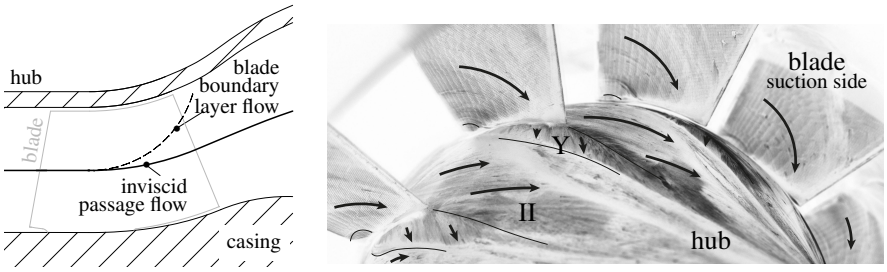

(a) Schematic streamlines

(b) Oil film flow at the hub and the blade's suction side, sym. blade, $\beta_S = 60^\circ$, rear perspective (II: passage vortex, Y: blade surface vortex)

Figure 8: The blade surface vortex in the duct of the VIGV with hub

2.3 Overall performance characteristics

Compared to the VIGV with open blade tips, much higher circumferential flow deflection rates were recorded for the vane with hub as shown in Figure 9(a). Even overturning $\Delta\beta_\Theta > 90 - \beta_S$ is observed for wide parts of $\bar{r}$. The significant deviations in $\Delta\beta_\Theta$ are explained by the different axial acceleration of the flow in the two configurations. Due to the reduced constriction of the free cross-sectional surface by only 4.8% instead of 32.7%, the mean averaged axial velocity c_{ax} downstream the VIGV is lower with applied hub. Significant deviations of $\Delta\beta_\Theta$ are hence reasonable at rather similar circumferential velocity levels of both cascades at equal stagger angles, see Figure 9(c). The significant overturning of $\Delta\beta_\Theta$ over the set metal angle is still remarkable, but can be explained by the conservation of angular momentum or

$$rc_u = \text{const} \tag{4}$$

at fairly constant meridional velocities (Gambini and Vellini, 2021, p. 51). To facilitate matters, inviscid fluid is assumed and an ideal shift of the streamlines from the radial position r_{x1} at the VIGV inlet to r_{x2} at the outlet is postulated. According to this, the local radius r_{xi} at the axial position i of an arbitrary streamline would follow a constant area ratio between r_{xi} and the local hub radius $d_i/2$ and the local cross section between the casing radius $D_i/2$ and $d_i/2$

$$\frac{\int_{d_i/2}^{r_{xi}} r dr}{\int_{d_i/2}^{D_i/2} r dr} = \text{const.} \quad \Longrightarrow \quad r_{x2} = \frac{1}{2}\sqrt{\frac{4r_{x1}^2 - d_1^2}{D_1^2 - d_1^2}\left(D_2^2 - d_2^2\right) + d_2^2}. \tag{5}$$

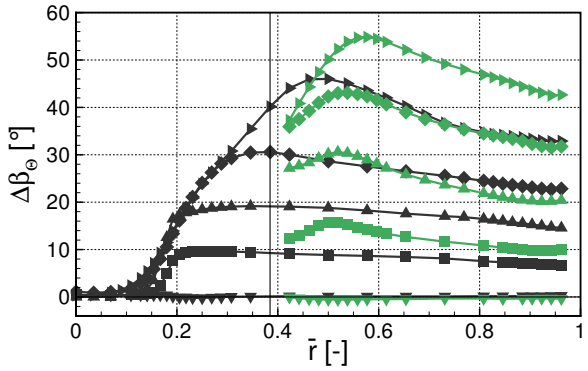

(a) Radial distribution of the circ. flow deflection $\Delta\beta_\Theta$

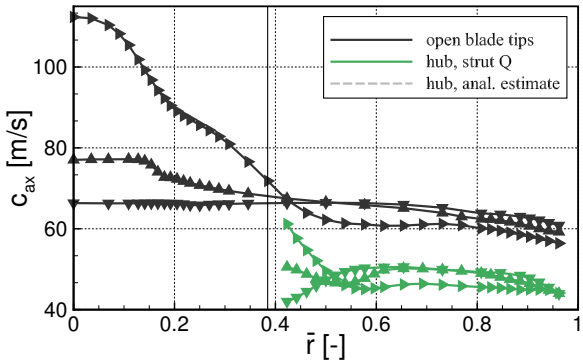

(b) Axial distribution of the circumferential velocity c_{ax}

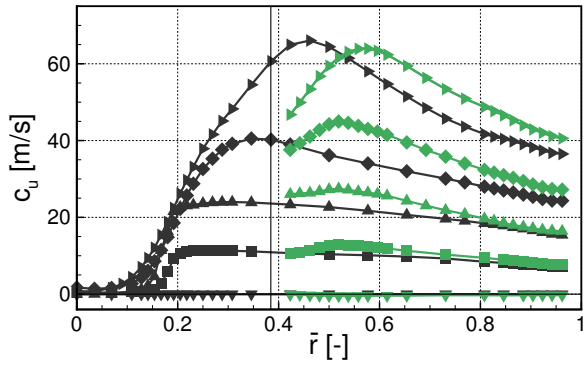

(c) Radial distribution of the circumferential velocity c_u

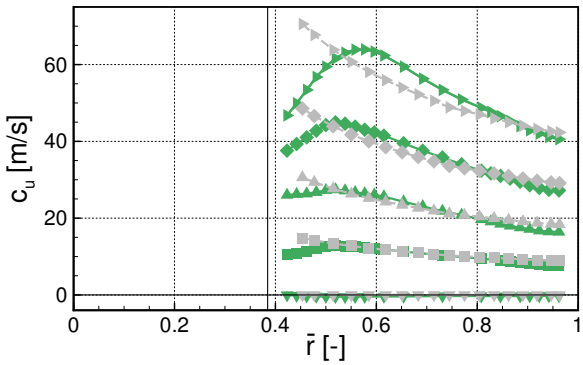

(d) Validity check of the circumferential velocity distribution c_u

Figure 9: Radial deflection characteristics of the customary VIGV with and without implemented hub, Symbols: β_S = 90° ▼, 80° ■, 70° ▲, 60° ◆, 50° ▶

D_i and d_i are also outlined in Figure 3(b). The circumferential flow velocity at the blade, in turn, is roughly estimated by the incoming axial velocity c_{ax1} and the set stagger angle β_S at

$$c_{u1} = c_{ax1} \tan\left(90^\circ - \beta_S\right). \tag{6}$$

Provided the conservation of angular momentum, the estimated radial position r_{x2}, and the estimation c_{u1} in Eq. 4 to 6, the expected circumferential flow deflection in the cross section b_1 can be predicted as

$$c_{u2} = \frac{r_{x1}}{r_{x2}} c_{ax1} \tan\left(90^\circ - \beta_S\right). \tag{7}$$

Although the neglect of radial equilibrium and the missing coverage of the decreased flow deflection rates near the hub at $\bar{r} \leq 0.5$ in Figure 9(d), the simplistic analytical estimate still underlines the trend of a rising circumferential velocity c_u towards lower radii. The influence of the hub or blow hole has not been considered by the simplistic model. Effects near the lowest radii are hence not reproduced.

The aspect of locally rising axial velocities near the hub at decreased stagger angles β_S as shown in Figure 9(b) is moreover interesting. Apart from an increased path length at increased swirl, the observed local acceleration and the thereby less adverse pressure gradients near the hub are considered responsible to suppress the hub separation at $\beta_S \leq 70^\circ$.

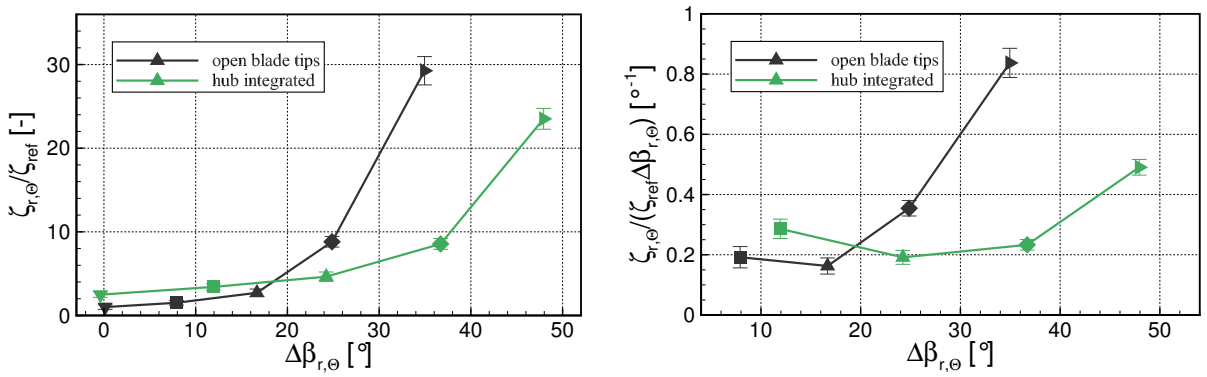

(a) Total pressure loss coefficient against the circumferential flow deflection

(b) Total pressure loss coefficient per circ. flow deflection against the circumferential flow deflection

Figure 10: Integral performance of the customary VIGV with hub compared to the setup with open blade tips, Symbols: β_S = 90° ▼, 80° ■, 70° ▲, 60° ◆, 50° ▶

To assess whether an overall improved performance gain can be obtained by the hub configuration, the integral losses are plotted in Figure 10(a) against the integral flow deflection. Whereas an increased circumferential flow deflection $\Delta\beta_{r,\Theta}$ based on a decreased axial acceleration and an avoided open flow separation at β_S = 60° promise improved deflection characteristics, total pressure losses rose by the drag of the struts as well as additional secondary flow effects induced by the hub. At high stagger angles the outlined drawbacks of the hub outweigh. Superior performance is, however, expected at decreased stagger angles. The present hub configuration reaches this tipping point at β_S = 70°. For the configuration with open blade tips, the operational limit has been set to β_S = 60° ($\Delta\beta_{r,\Theta} \approx 25°$). Accordingly, the efficient vane operation is increased by the hub by more than ten degrees to $\Delta\beta_{r,\Theta} \approx 35°$. The outlined trend is substantiated by the consideration of the relative losses per flow deflection in Figure 10(b). The performance curve of the configuration with hub is kept low until the open flow separation sets in at β_S = 50°.

3 Conclusions and Outlook

The objective of the present paper is the comparison of the aerodynamic performance of the two, typical axial VIGV designs with either open blade tips or hub. Two VIGVs with an identical casing and blade contour were assessed by five-hole probe wake field measurements and oil film flow visualisations.

The evaluation of the wake fields revealed a variation of the total pressure losses generated by both configurations. If a hub was applied, secondary flow losses at the casing shifted, presumably due to the lower constriction of the cross-sectional area, further away from the wall. Significant secondary flow losses moreover arose near the hub wall, which surpass the limited losses of the open blade tip vortex. An additional suction sided vortex structure near the hub is moreover found to rotate inversely to a passage vortex. The vortex is considered akin to the blade surface vortex of centrifugal inducers. According to expectations, the onset of the open flow separation on the suction side shifts by the shorter blade height and the larger minimum local Reynolds number Re_c of the hub configuration to β_S < 60°. At β_S = 50°, the flow still stalls. Solely the blade flow in the wakes of the four struts remains attached. The shifted onset of open flow separation is accounted to the increased turbulence level within the strut wake.

The operational limits of the overall vane are still defined by the arising stall at the remaining blades.

Considering the mean averaged total pressure losses against the obtained flow deflection, the vane with open blade tips remains superior for the generation of low swirl rates. This is to be expected by the avoided losses by struts and the hub wall. At $\beta_S \approx 70^\circ$, the trend reverses and the hub configuration becomes favourable. Apart from avoided open flow separation mechanisms at $\beta_S = 60^\circ$, significantly enhanced deflection angles in the exit plane b_1, which even exceed the metal angle of the blade, are therefore accounted. One reason for the high deflection angles is the reduced axial acceleration of the flow in the VIGV. The second effect, which also explains the overshooting of the blade metal angle is the radial shift of the fluid flow along with a continuity of angular momentum. Accordingly, open blade tips are to be preferred in compressor applications, which neither call for a wide operating range nor frequent off-design conditions. The hub, in turn, provides advantages if a high compressor flexibility is required.

Apart from the optimisation of the contour of the hub and casing, more advanced blade geometries are a reasonable option to further improve the operating range of both investigated VIGV designs. Substantial improvements by a variable, split blade design have been proven by Frank et al. (2022b) for the vane with open blade tips. Corresponding measurements are pending for the configuration with hub. In accordance with the previous study, suppressed open flow separation effects beyond the currently limiting stagger angles of $\beta_S = 50^\circ$ can be expected by the split blade.

ACKNOWLEDGEMENTS

The authors gratefully acknowledge the financial support of the Kopernikus project SynErgie by the German Federal Ministry of Education and Research (BMBF) and the project supervision by the project management organization Projektträger Jülich (PTJ). The project was performed in collaboration with MAN Energy Solutions SE. Special thanks go to Jan Klausmann at MAN for valuable support. His contributions are highly acknowledged here.

REFERENCES

M. Coppinger and E. Swain. Performance Prediction of an Industrial Centrifugal Compressor Inlet Guide Vane System. *Proceedings of the Institution of Mechanical Engineers*, 214(A), 2000.

D. Eckardt. Detailed Flow Investigations Within a High Speed Centrifugal Compressor Impeller. *J. Fluids Eng.*, 98(3), 1976.

W. Fister. *Fluidenergiemaschinen - Band 2: Auslegung, Gestaltung, Betriebsverhalten ausgewählter Verdichter- und Pumpbauarten*. Springer-Verlag, Berlin Heidelberg, 1986. ISBN 3-540-15478-7.

R. G. Frank, C. Wacker, and R. Niehuis. A New Test Facility for Advanced Testing of Variable Inlet Guide Vanes. MTT2520A18. MTT Measuring Techniques in Turbomachinery, 2020.

R. G. Frank, C. Wacker, and R. Niehuis. Loss Characterization of a Conventional Variable Inlet Guide Vane. *Int. J. Turbomach. Propuls. Power*, 6(30), 2021.

R. G. Frank, N. Seer, H. Wegner, and R. Niehuis. On the Loss Behaviour of a Split Blade VIGV Configuration at Varied Stagger Angle Combinations. 249. International Society of Air Breathing Engines, 2022a.

R. G. Frank, C. Wacker, and R. Niehuis. Loss Characterization of Advanced VIGV Configurations with Adjustable Blade Geometry. *J. Turbomach.*, 144(3), 2022b.

M. Gambini and M. Vellini, editors. *Turbomachinery - Fundamentals, Selection and Preliminary Design*. Springer Nature Switzerland AG, Cham, 2021. ISBN 978-3-030-51298-6.

D. Händel. Untersuchungen der Verlustcharakteristik und des Umlenkverhaltens eines Eintrittsleitapparates zur

Vordrallregelung mit symmetrischem Profil und variablem Staffelungswinkel am Gitter V410. LRT-WE12-16/05. Institute of Jet Propulsion, University of the Bundeswehr Munich, 2016.

D. Händel, S. Barthmes, and R. Niehuis. 2D Investigation of the Flow Through a Symmetric Variable Inlet Guide Vane, Part 1: Experimental Analysis. AIAA 2013-3682. AIAA/ASME/ASE/ASEE Joint Propulsion Conference, 2013.

D. Händel, R. Niehuis, and U. Rockstroh. Aerodynamic Investigation of a Variable Inlet Guide Vane With Symmetric Profile. GT2014-26900. ASME Turbo Expo, 2014.

D. Händel, R. Niehuis, and J. Klausmann. Aerodynamic Investigation of an Advanced VIGV Design of Adjustable Geometry for Very High Flow Turning. GT2015-42166. ASME Turbo Expo, 2015.

J. Hourmouziadis. Aerodynamic Design of Low Pressure Turbines. AGARD-LS-167. Advisory Group for Aerospace Research and Development, 1989.

M. Ishino, Y. Iwakiri, A. Bessho, and H. Uchida. Effects of Variable Inlet Guide Vanes on Small Centrifugal Compressor Performance. 99-GT-157. ASME Turbo Expo, 1999.

R. E. Mayle. The 1991 IGTI Scholar Lecture: The Role of Laminar-Turbulent Transition in Gas Turbine Engines. *J. Turbomach.*, 113(4), 1991.

A. Mohseni, E. Goldhahn, R. A. Van den Braembussche, and J. R. Seume. Novel IGV Designs for Centrifugal Compressors and Their Interaction with the Impeller. *J. Turbomach.*, 134(2), 2012.

J. M. Sanz, E. R. McFarland, N. L. Sanger, T. F. Gelder, and R. H. Cavicchi. Design and Performance of a Fixed, Nonaccelerating Guide Vane Cascade That Operates Over an Inlet Flow Angle Range of 60 Deg. *J. Eng. Gas Turbines Power.*, 107(2), 1985.

A. Sauer, E. Abele, and H. U. Buhl, editors. *Energieflexibilität in der deutschen Industrie - Band 1: Ergebnisse aus dem Kopernikus-Projekt SynErgie*. Frauenhofer Verlag, Stuttgart, 2019. ISBN 978-3-8396-1479-2.

A. Sauer, H. U. Buhl, A. Mitsos, and M. Weigold, editors. *Energieflexibilität in der deutschen Industrie - Band 2: Markt- und Stromsystem, Managementsysteme und Technologien energieflexibler Fabriken*. Frauenhofer Verlag, Stuttgart, 2022. ISBN 978-3-8396-1778-6.

O. P. Sharma and T. L. Butler. Predictions of Endwall Losses and Secondary Flows in Axial Flow Turbine Cascades. *J. Turbomach.*, 109(2), 1987.

C. H. Sieverding. Recent Progress in Understanding of Basic Aspects of Secondary Flows in Turbine Blade Passages. *J. Eng. Gas Turbines Power*, 107(2), 1985.

H. Simon, T. Wallmann, and T. Mönk. Improvements in Performance Characteristics of Single-Stage and Multistage Centrifugal Compressors by Simultaneous Adjustments of Inlet Guide Vanes and Diffuser Vanes. *J. Turbomach.*, 109(41), 1987.

S. A. Sjolander. Overview of Tip-Clearance Effects in Axial Turbines. VKI LS 1997-01. Von Karman Institute for Fluid Dynamics, 1997.

U. Stark and M. Böhle. Theoretische und experimentelle Untersuchungen an ungestaffelten Gittern aus Profilen mit mechanischen Klappen. *Forschung im Ingenieurwesen*, 56(6), 1990.

E. S. Taylor. Film Notes for Secondary Flow. 21612. Education Development Center, Inc., 1968.

A. Tesch, J. Ortsmanns, M. Lange, E. Johann, K. Vogeler, and V. GÃ¼mmer. An experimental investigation of a tandem stator flow characteristic in a low speed axial research compressor. GT2014-26104. ASME Turbo Expo, 2014.

D. Weihs and J. Katz. Cellular Patterns in Poststall Flow over Unswept Wings. *AIAA J.*, 21(12), 1983.

A. E. Winkelmann and J. B. Barlow. Flowfield Model for a Rectangular Planform Wing beyond Stall. *AIAA J.*, 18 (8), 1980.